Electronic and magnetic properties of single-layer $FeCl_2$ with defects

E. Ceyhan,[1] M. Yagmurcukardes,[1,2,3,*] F. M. Peeters,[3] and H. Sahin[1]
[1]*Department of Photonics, Izmir Institute of Technology, 35430 Izmir, Turkey*
[2]*NANOlab Center of Excellence, Groenenborgerlaan 171, B-2020 Antwerp, Belgium*
[3]*Department of Physics, University of Antwerp, Groenenborgerlaan 171, B-2020 Antwerp, Belgium*

(Received 20 July 2020; revised 13 October 2020; accepted 22 December 2020; published 12 January 2021)

The formation of lattice defects and their effect on the electronic properties of single-layer $FeCl_2$ are investigated by means of first-principles calculations. Among the vacancy defects, namely mono-, di-, and three-Cl vacancies and mono-Fe vacancy, the formation of mono-Cl vacancy is the most preferable. Comparison of two different antisite defects reveals that the formation of the Fe-antisite defect is energetically preferable to the Cl-antisite defect. While a single Cl vacancy leads to a $1\mu_B$ decrease in the total magnetic moment of the host lattice, each Fe vacant site reduces the magnetic moment by $4\mu_B$. However, adsorption of an excess Cl atom on the surface changes the electronic structure to a ferromagnetic metal or to a ferromagnetic semiconductor depending on the adsorption site without changing the ferromagnetic state of the host lattice. Both Cl-antisite and Fe-antisite defected domains change the magnetic moment of the host lattice by $-1\mu_B$ and $+3\mu_B$, respectively. The electronic ground state of defected structures reveals that (i) single-layer $FeCl_2$ exhibits half-metallicity under the formation of vacancy and Cl-antisite defects; (ii) ferromagnetic metallicity is obtained when a single Cl atom is adsorbed on upper-Cl and Fe sites, respectively; and (iii) ferromagnetic semiconducting behavior is found when a Cl atom is adsorbed on a lower-Cl site or a Fe-antisite defect is formed. Simulated scanning electron microscope images show that atomic-scale identification of defect types is possible from their electronic charge density. Further investigation of the periodically Fe-defected structures reveals that the formation of the single-layer $FeCl_3$ phase, which is a dynamically stable antiferromagnetic semiconductor, is possible. Our comprehensive analysis on defects in single-layer $FeCl_2$ will complement forthcoming experimental observations.

DOI: 10.1103/PhysRevB.103.014106

I. INTRODUCTION

Since the synthesis of graphene [1], two-dimensional (2D) ultrathin materials have gained significant attention due to the outstanding properties achieved by the confinement of charge carriers in one direction. Accordingly, recent research efforts have been devoted to the demonstration of magnetism at the 2D limit. Novel magnetic ultrathin materials, such as the 2D ferromagnetic (FM) semiconductors CrI_3 [2–4] and $Cr_2Ge_2Te_6$ [5], have been successfully synthesized. In addition, other 2D magnetic single layers such as $RuCl_3$ [6,7], VSe_2 [8,9], $FePS_3$ [10], ultrathin layers of metal phosphorus trichalcogenides [11], $MnSe_2$ [12], and VCl_3 [13] have been added to the library of 2D magnets. Research on this class of material is still continuing to find novel 2D magnetic crystal structures with better stability and different functionalities.

$FeCl_2$, a member of the family of magnetic transition-metal halides (TMHs), in its bulk form consists of weakly interacting ferromagnetic layers exhibiting weak interlayer antiferromagnetism [14,15]. Moreover, the ultrathin single-layer form of $FeCl_2$ was theoretically predicted to possess dynamical stability in its 1T-phase (in which Fe-layer is sandwiched between two Cl-layers) as a free-standing layer [16]. It was reported that single-layer $FeCl_2$ has a FM ground state giving rise to half-metallic behavior and making it an important candidate for spintronic and optoelectronic applications. Another study showed that controlling the magnetic anisotropy of single-layer $FeCl_2$ can be realized via charging and doping, and this can lead to the emergence of tunable and switchable magnetic functionalities [17]. In addition, Zheng *et al.* reported that while the FM ground state of 1T-$FeCl_2$ is robust, the magnetic anisotropy energy increases with applied strain [18]. Very recently, the single-layer form of $FeCl_2$ was experimentally demonstrated using molecular beam epitaxy (MBE) on Au(111) and graphite substrates [19]. The formation of the 1T-phase of $FeCl_2$ either in single-layer or in few-layer form was revealed by high-resolution scanning tunneling microscopy (STM) measurements.

It has been demonstrated that defects play an important role in tailoring electronic, mechanical, and optical properties of materials, especially in their 2D limit [20–24]. Studies on graphene revealed that many different types of defects, such as point defects (vacancies, substitutional dopings, or atomic adsorption), and line defects are favorable, depending on the experimental growth conditions [25]. Zhou *et al.* reported the observation of several defect types in single-layer MoS_2, and it was shown that due to its three-atom-thick structure, created grain boundaries are more complex than those in graphene, and they lead to the formation of 1D metallic wires in a 2D

*Corresponding author: mehmetyagmurcukardes.edu@gmail.com

semiconducting MoS_2 layer [22]. On the other hand, Hong *et al.* reported that Mo-S antisite defects induce local magnetism in a nonmagnetic MoS_2 layer leading to the creation of nearly midgap states [26]. In addition, defect engineering in 2D magnetic structures has been shown to tailor the magnetic and electronic properties of the material. It was also shown that single-layer CrI_3 undergoes a phase transition via the creation of point defects [27,28].

Motivated by the recent experimental realization of magnetic single-layer $FeCl_2$ [19], we investigated the effect of defects on the structural and electronic properties of single-layer $FeCl_2$. Our results reveal that while some types of defects preserve the half-metallic nature of single-layer $FeCl_2$, a transition to ferromagnetic-semiconductor and ferromagnetic-metal states is also possible upon defect formation. In addition, we showed that the creation of dense Fe-vacancies results in the formation of dynamically stable single-layer $FeCl_3$ displaying an antiferromagnetic semiconducting ground state.

II. COMPUTATIONAL METHODOLOGY

When determining the optimized structures of defected single-layer $FeCl_2$ crystals and the resulting electronic features, *ab initio* calculations were performed using the Vienna *ab initio* simulation package (VASP) [29,30]. To describe exchange-correlation interactions, the Perdew-Burke-Ernzerhof (PBE) [31] form of the generalized gradient approximation (GGA) was adopted. The kinetic energy cutoff for a plane-wave basis was taken to be 500 eV. The optimization criteria for the energies and the forces on the individual atoms were taken to be 10^{-6} eV and 10^{-5} eV/Å, respectively. The width of Gaussian smearing was chosen to be 0.05 eV when calculating the partial density of states (PDOS). For the structural optimization and the PDOS calculations of an 108-atom $FeCl_2$ supercell, $2 \times 2 \times 1$ and $3 \times 3 \times 1$ Γ centered k-point samplings were used, respectively. To avoid interlayer interaction between adjacent layers, at least a 15 Å vacuum space was inserted in the out-of-plane direction. To obtain a visual description of the influence of the defects on the structural properties, STM images were also calculated. The tip distance was taken to be 1.5 Å, a reliable tip distance obtained from the experimental images of bare $FeCl_2$. The energy range for the STM images was -2 to 0 eV for the valence states.

III. DEFECT-INDUCED RELAXATIONS AND RECONSTRUCTIONS IN SINGLE-LAYER $FeCl_2$

To avoid defect-defect interactions, a large 108-atom supercell is considered, and a total of nine different types of defects are investigated: (i) mono-Cl vacancy: V_{Cl}; (ii) di-Cl vacancy: V_{2Cl}; (iii) three-Cl vacancy: V_{3Cl}; (iv) mono-Fe vacancy: V_{Fe}; (v) single Cl adsorption on top of upper-Cl: $T_{Cl\text{-}up}$; (vi) single Cl adsorption on lower-Cl: $T_{Cl\text{-}down}$; (vii) single Cl adsorption on an Fe atom: T_{Fe}; (viii) an Fe atom replacing a Cl atom: Fe-antisite; and (ix) a Cl atom replacing an Fe atom: Cl-antisite (see Fig. 1).

Single-layer $FeCl_2$ in 1T-phase consists of sixfold-coordinated Fe atoms sandwiched between Cl layers. The optimized in-plane lattice parameters of a hexagonal primitive unit cell of $FeCl_2$ are $a = b = 3.47$ Å. For the optimized defected structures, the expansion or the compression rate of the lattice is calculated with respect to the lattice parameter of bare $6 \times 6 FeCl_2$. As shown in Table I, most of the defects lead to shrinkage in the lattice, while the Cl-antisite defect locally enlarges the host lattice (+0.5%). The structural optimizations reveal that in addition to the local distortions around the defect site, there also exist long-range distortions in the host lattice. Apparently, in structures of Cl-vacancies, an Fe-antisite defect, and single Cl adsorption on the lower Cl atom, Fe atoms are found to be distorted and form trimer units due to asymmetric reconstruction of the atoms facing the defect site. In contrast, as the atoms are redistributed symmetrically in the defect site, the symmetry of the host lattice is found to be conserved. Therefore, we note that asymmetric reconstructions of the defect environment create Peierls-like lattice distortions in the host lattice. In addition, defected crystal structures of V_{Fe} and T_{Fe} have the same lattice parameters as that of defect-free structure. To compare the energetics of defects, the formation energies are calculated using the equation $E_{for} = E_{defected} - E_{bare} \pm \sum n_i E_i$, where $E_{defected}$ and E_{bare} stand for the total energies of the defected and bare $FeCl_2$ single layers, respectively, while n_i and E_i represent the total number and the total energy of the vacant or added atom. Note that for the adsorbed (vacant) atoms, $-$ (+) signs are considered, respectively. Therefore, negative values of E_{for} imply that the formation of a defect of a bonded extra atom over the $FeCl_2$ surface (adsorption) is favorable.

TABLE I. For the single-layer defected 1T-$FeCl_2$, we present the type of defect; the expansion rate of the lattice parameter ($-$ and + stand for compression and expansion, respectively), Δa; the defect formation energy, E_{for}; the net magnetic moment of the defect domain, $\Delta\mu$; the magnetic/electronic ground state; and the energy band gap of FM semiconducting states, E_{gap}. Note that formation energies for Cl-vacancies are given in eV/Cl in order to be comparable.

Defect type	Δa (%)	E_{for} (eV)	$\Delta\mu$ (μ_B)	Magnetic/electronic Ground state	E_{gap} (eV)
V_{Cl}	−0.6	0.02	−1	Half-metal	
V_{2Cl}	−0.9	1.23	−2	Half-metal	
V_{3Cl}	−1.0	1.12	−3	Half-metal	
V_{Fe}	0.0	0.98	−4	Half-metal	
$T_{Cl\text{-}up}$	−0.3	1.78	0	FM/metal	
$T_{Cl\text{-}down}$	−0.5	0.70	0	FM/semiconductor	0.18
T_{Fe}	0.0	1.90	0	FM/metal	
Cl-antisite	+0.5	3.36	−1	Half-metal	
Fe-antisite	−0.6	2.91	+3	FM/semiconductor	0.43

The formation energies of the Cl-vacancies are given in eV/Cl in order to make a comparison possible between the different vacancies. Notably, the choice of the chemical potential of the individual atoms is considered in the Fe-rich limit. We use the relation $\mu_{Fe} + 2\mu_{Cl} = \mu_{FeCl_2}$, where μ_{Fe}, μ_{Cl}, and μ_{FeCl_2} stand for the total energies of Fe, Cl, and single-layer $FeCl_2$, respectively. At the Fe-rich limit, the chemical potential of the Fe atom is calculated using the ferromagnetic bulk form of Fe. Using μ_{Fe} from Fe-bulk form, μ_{Cl} is calculated from the total energy of single-layer $FeCl_2$. The formation energies of V_{Cl}, V_{2Cl}, and V_{3Cl} vacancies are calculated to be

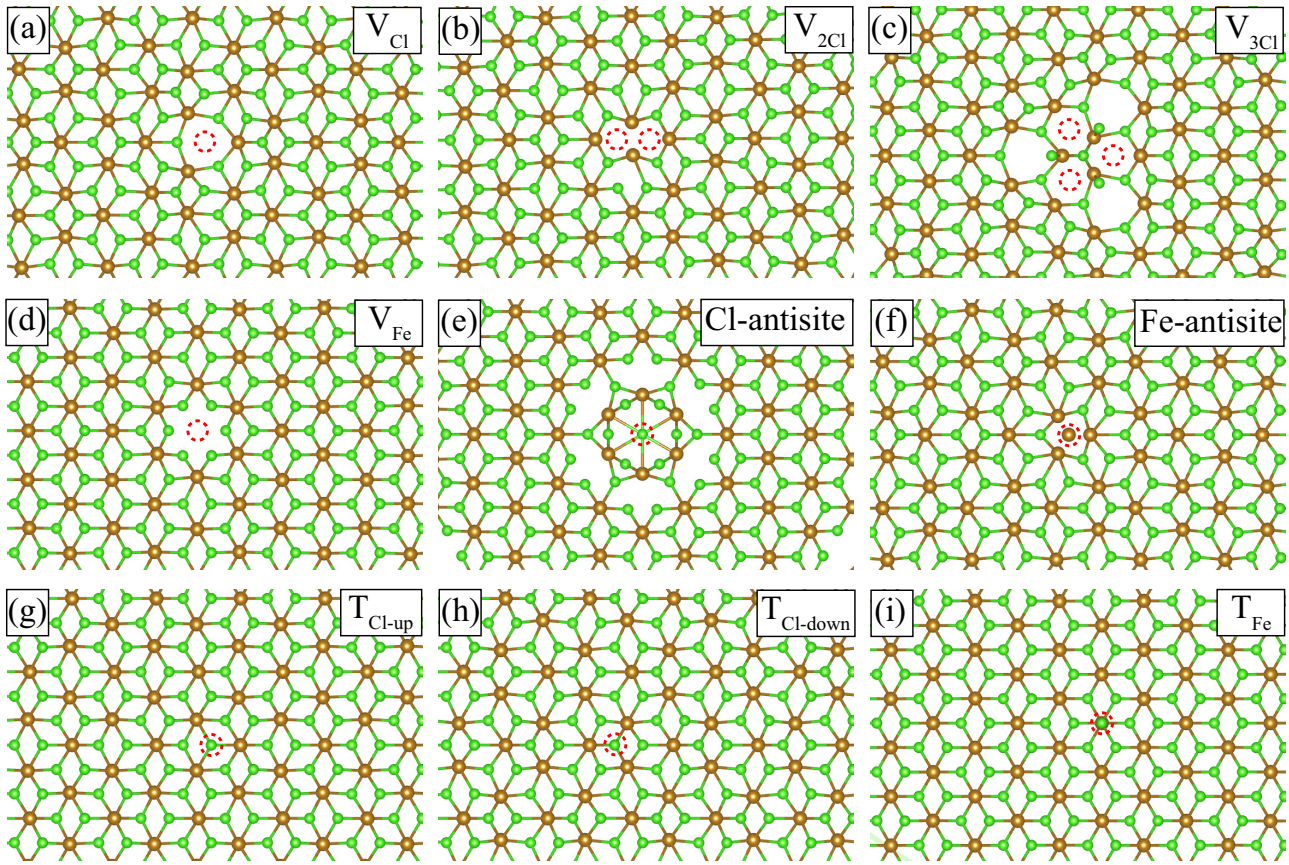

FIG. 1. Top view of single-layer $FeCl_2$ for the defect types: (a) Mono- (V_{Cl}), (b) di- (V_{2Cl}), (c) three-Cl (V_{3Cl}), and (d) mono-Fe (V_{Fe}) vacancies. Also shown are the antisite defects of (e) Cl substituted in a Fe site (Cl-antisite) and (f) Fe substituted in a Cl site (Fe-antisite), and adsorption of a single Cl atom on top of (g) upper-Cl ($T_{Cl\text{-}up}$), (h) lower-Cl ($T_{Cl\text{-}down}$), and (i) Fe-atom (T_{Fe}). The dashed red circles represent the vacant or added atoms in the structure.

0.02, 1.23, and 1.12, respectively. Apparently, the formation of single vacancies is more favorable than that of multiple Cl vacancies. Note that the formation of a divacancy that allows stronger bonding between surrounding Fe atoms is more favorable than that of a triple Cl vacancy. In addition, compared to single Cl, the formation of a single Fe vacancy (V_{Fe}) is more favorable than the formation of multiple Cl vacancies (0.98 eV). On the other hand, the formation of an Fe-antisite defect (2.91 eV) is found to be energetically preferable as compared to Cl-antisite formation (3.36 eV) as a result of the magnetic nature of an Fe atom. As a single Cl atom is adsorbed on single-layer $FeCl_2$, the adsorption energies are found to be 1.78, 0.70, and 1.90 eV for the T_{Fe}, $T_{Cl\text{-}up}$, and $T_{Cl\text{-}down}$ sites, respectively. Apparently, the energy required to form Cl adsorption on the top of a lower Cl atom is lowest since the adsorbed Cl atom tends to come closer to the layer surface. In addition, a comparison of single Cl adsorption with that of a graphene layer (1.16 eV) [32] reveals stronger Cl adsorption on the $FeCl_2$ surface.

IV. MONITORING DEFECTS IN SINGLE-LAYER $FeCl_2$ BY A SCANNING TUNNELING MICROSCOPE IMAGE

STM measurements, which provide atomically precise information about the crystal structure, are important for imaging surfaces. We present calculated STM images for nine different vacancy types in Fig. 2. First of all, it is obviously seen that Fe-originated electronic states dominate the DOS of the bare single-layer $FeCl_2$, and hence they lead to the emergence of bright spots in the STM image. In the case of V_{Cl} [Fig. 2(a)], a dark spot surrounded by three Fe atoms makes the defect domain visibly distinct from the host lattice. For the case when two neighboring Cl atoms are removed, V_{2Cl}, the two Fe atoms around the defect domain tend to form a Fe_2-dimer that is slightly brighter than the Fe atoms of the host lattice. However, for the case of V_{3Cl}, the lattice reconstruction leads to a bright center-triangle formed by three Fe atoms. As shown in Fig. 2(d), differing from a single Cl vacancy, the presence of a single Fe vacancy leads to a dark spot surrounded by six bright spots of the host lattice. The antisite defects are also found to exhibit distinctive STM images reflected by the inclusion of extra Fe or Cl atoms at the defect site. In the Cl-antisite defected structure [Fig. 2(e)], an extra Cl atom appears as a red dot at the center of the surrounding six Cl atoms. The red color of the seven Cl atoms can be attributed to their positions in the out-of-plane direction. In the optimized structure, the seven Cl atoms are found to be at a higher position and thus closer to the tip in STM simulation. On the other hand, in the Fe-antisite structure, the extra Fe atom occurs at a higher position than those of the surrounding three Fe atoms. It is clear from the STM image that the extra Fe atom is brighter than the Fe atoms of the host lattice.

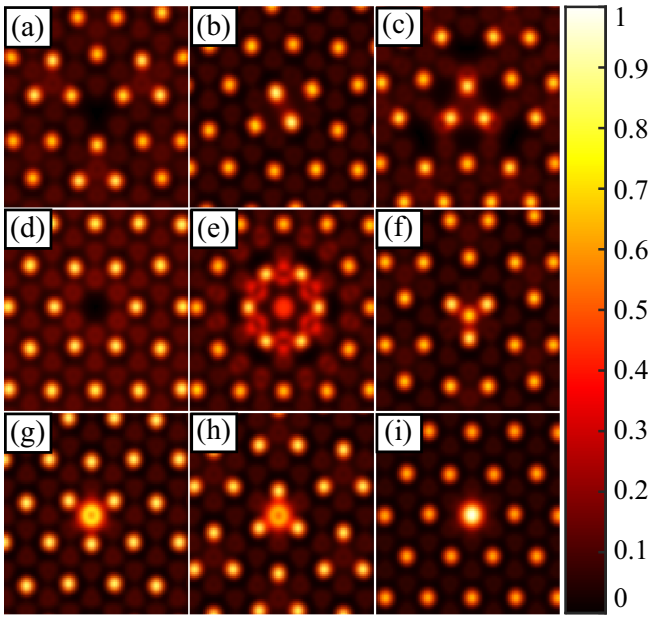

FIG. 2. Simulated STM images of single-layer $FeCl_2$ of (a) V_{Cl}, (b) V_{2Cl}, (c) V_{3Cl}, and (d) V_{Fe} vacancies. (e) Cl-antisite and (f) Fe-antisite defected structures. Adsorption of a single Cl atom at (g) $T_{Cl\text{-}up}$, (h) $T_{Cl\text{-}down}$, and (i) T_{Fe} sites, respectively.

Moreover, the single-Cl adsorption on three different sites can be clearly distinguished through the STM images. The vertical position of the adsorbed Cl atom affects its brightness such that it appears less bright when adsorbed on top of the lower Cl atom [Fig. 2(h)]. As it is adsorbed on a Fe atom, the Cl atom enhances the brightness of the Fe atom.

V. ELECTRONIC AND MAGNETIC PROPERTIES

For investigation of how electronic and magnetic properties of single-layer $FeCl_2$ are modified, we calculated the partial electronic density of states (PDOS) as shown in Fig. 3. Single-layer 1T-$FeCl_2$ has a half-metallic ground state with a 4.30 eV energy gap for minority states while the Fermi level is crossed by Fe-dominated majority states. Notably, there is disagreement between theoretical reports about whether $FeCl_2$ is a half-metal or an insulator. While it was reported to be an insulator with the inclusion of spin-orbit interaction [33], Torun *et al.* have shown that $FeCl_2$ is a half-metal [16]. In a recent experiment, Cai *et al.* demonstrated that single-layer $FeCl_2$ synthesized on highly oriented pyrolytic graphite is an insulator [34]. However, it was mentioned in the study that the half-metallic behavior of a free-standing $FeCl_2$ layer cannot be excluded since there is a charge transfer from graphite to $FeCl_2$, which shifts the Fermi level and induces a gap in $FeCl_2$. Therefore, there is not any experimental observation of the electronic behavior of free-standing single-layer $FeCl_2$. The rest of our paper investigates the effect of defects on the properties of half-metallic free-standing $FeCl_2$. Our results reveal that Cl- and Fe-vacancies and the Cl-antisite defect structures exhibit half-metallic behavior. In contrast, for single Cl adsorbed at $T_{Cl\text{-}up}$ and T_{Fe} structures, Cl adatom-induced midgap states contribute both majority and minority states around the Fermi level and therefore result in a transition from

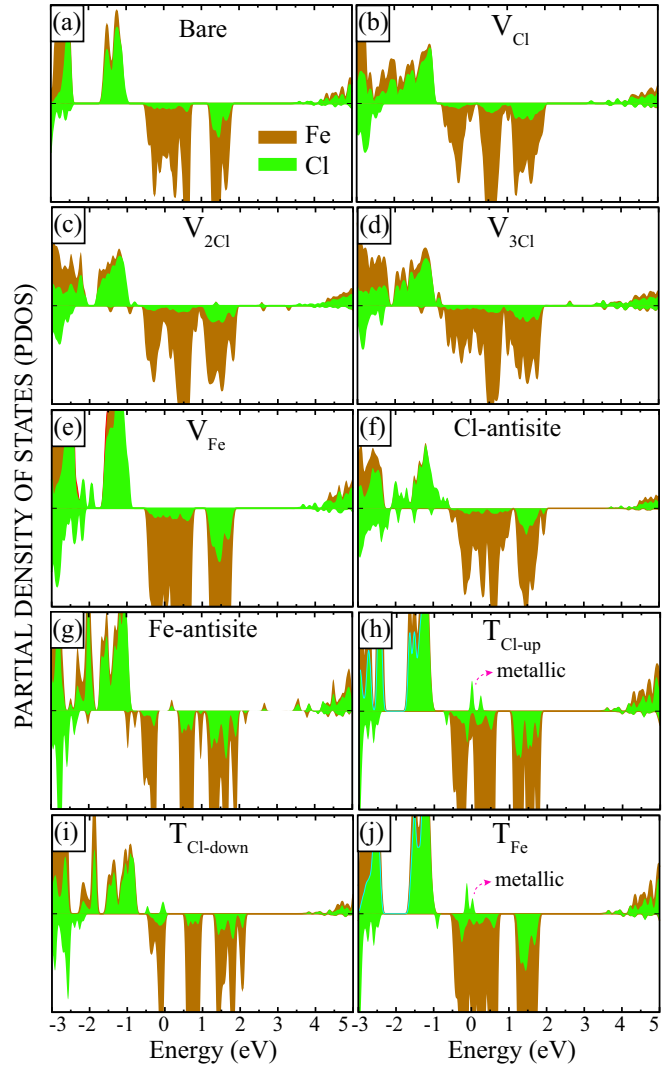

FIG. 3. The partial density of states (PDOS) for the defected structures; (a) bare, (b) V_{Cl}, (c) V_{2Cl}, (d) V_{3Cl}, (e) V_{Fe}, (f) Cl-antisite, (g) Fe-antisite, (h) $T_{Cl\text{-}up}$, (i) $T_{Cl\text{-}down}$, and T_{Fe}.

a half-metallic to a FM metallic state. On the other hand, the Fe-antisite and the Cl adsorbed at $T_{Cl\text{-}down}$-type defects lead to a band-gap opening and FM semiconducting behavior with a tiny energy band gap of 0.43 and 0.18 eV, respectively. Electronic band dispersions of these defects are shown in Fig. 4. In the case of an Fe-antisite defect, single-layer $FeCl_2$ is found to exhibit an indirect gap with its valence- and conduction-band edges residing at the K and Γ points, respectively. On the other hand, an adsorbed Cl atom at the $T_{Cl\text{-}down}$ site induces midgap states, which are flat, nondispersive, and located below and above the Fermi level. The electronic band gap between the midgap states is found to be 0.18 eV. Our findings reveal the tunable electronic and magnetic behavior of $FeCl_2$ via defect formation from half-metal to semiconductor and even to metal. Thus, depending on the formed defect type, single-layer $FeCl_2$ can be used in different electronic device applications.

We now discuss the effect of local magnetism induced by the defect domain on the host lattice. In the crystal structure of defect-free single-layer $FeCl_2$, Fe atoms ferromagnetically

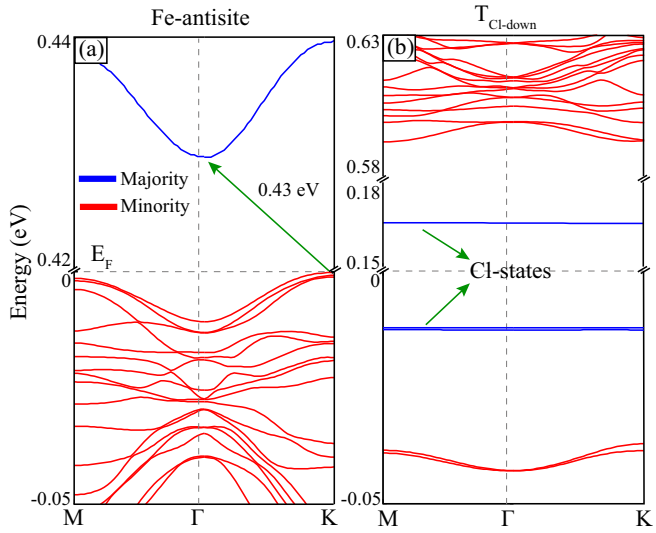

FIG. 4. Electronic band structures of (a) Fe-antisite and (b) $T_{Cl\text{-}down}$ defected $FeCl_2$. The Fermi energy is set to 0 eV. Blue and red solid lines represent opposite spin states, respectively.

couple to each other. As listed in Table I, the net magnetic moment of a defect domain (in $\Delta\mu$) is calculated in order to deduce its magnetic coupling type to the host lattice. It is calculated that for the adsorption of single Cl and Fe atoms, the magnetic moment of the defected domain is zero and has no contribution to the FM host lattice. In contrast, the defect domains of the four different vacancy types and that of the Cl-antisite structures lead to a decrease in the total magnetic moment of the structure. Specifically, V_{Cl} leads to a $\Delta\mu$ of $-1\mu_B$, and depending on the number of missing Cl atoms, it doubles (triples) for V_{2Cl} (V_{3Cl}) defect domains. On the other hand, V_{Fe} results in a local magnetic moment of $-4\mu_B$, which is compatible with the magnetic moment of the isolated Fe atom. The $\Delta\mu$ associated with the defect domain of Cl-antisite is found to be $-1\mu_B$. In contrast, the defect domain of Fe-antisite induces a $\Delta\mu$ of $+3\mu_B$ positively contributing to the ferromagnetism of the host lattice due to the presence of an additional Fe atom. The latter can be treated as the total contribution of single-Fe ($+4\mu_B$) substituted at a V_{Cl} ($-1\mu_B$) site giving rise to an additional magnetic moment of $+3\mu_B$. Apparently, the creation of defects induces local magnetic moments altered by the deviations from the nominal stoichiometry. Different magnetic coupling of defect environments to the host lattice for different defect formations may lead to various applications of single-layer $FeCl_2$ in spintronics.

VI. PERIODICALLY DEFECTED $FeCl_2$: FORMATION OF NOVEL STABLE $FeCl_3$ STRUCTURES

The formation of local domains composed of periodically defected crystal islands is possible during either the growth process or electron beam irradiation at high temperature. As shown in Fig. 5(a), introduction of symmetric Fe-vacancies in single-layer $FeCl_2$ leads to the formation of single-layer $FeCl_3$. Note that the stability and formation of single-layer $FeCl_3$ were also predicted in previous studies [35–37]. For the optimized atomic structure of single-layer $FeCl_3$, which can be viewed as a $\sqrt{3} \times \sqrt{3}$ supercell of single-layer $FeCl_2$ with point Fe-vacancies, cohesive energy is calculated to be 3.23 eV/at. Single-layer $FeCl_3$ belongs to the space group $C2/m$ with the optimized in-plane lattice parameters of 6.08 Å giving rise to the Fe-Cl bond length of 2.39 Å, which is smaller than that of $FeCl_2$ (2.46 Å).

To investigate the magnetic ground state of $FeCl_3$, FM and AFM interactions are taken into account, with the latter exhibiting three different configurations. Total energy optimizations reveal that AFM ordering, in which each Fe-pair exhibits opposite magnetic moments, is the ground-state magnetic configuration for single-layer $FeCl_3$. As shown in Fig. 5(b), the phonon dispersion reveals that the phononic vibrations of single-layer $FeCl_3$ are free from any imaginary eigenfrequencies indicating the dynamical stability of the structure.

On the other hand, electronic band structure of $FeCl_3$ shown in Fig. 5(c) reveals the indirect band-gap semiconducting nature with an AFM magnetic state. For single-layer $FeCl_3$, the electronic band gap is calculated to be 0.73 eV, where valence- and conduction-band edges reside at the K-Γ and Γ points, respectively. In addition, the partial density of states indicates that the top valence states are formed by both Fe and Cl orbitals while the lowest conduction states mainly arise from Fe-orbitals. Apparently, the created single-layer $FeCl_3$ stoichiometry possesses electronic and magnetic features that are distinct from the $FeCl_2$ structure.

VII. CONCLUSIONS

In the present study, the effect of defect formation on the electronic properties of a FM single-layer of $FeCl_2$ is investigated by means of first-principles calculations. Our results reveal that the formation of V_{Cl} and the Fe-antisite defects are the most preferable defects among vacancies and antisite defects, while adsorption of a single Cl atom on a lower Cl site has the highest formation energy. The magnetic moment of the host lattice is modulated by the defect domains (vacancies and antisite defects). On the other hand, various defect formations are shown to turn the half-metallic nature of $FeCl_2$ into a FM metallic state ($T_{Cl\text{-}up}$ and T_{Fe}) and even into FM semiconducting behavior ($T_{Cl\text{-}down}$ and Fe-antisite) while the half-metallic nature remains the same via vacancy and Cl-antisite formations. Furthermore, by forming periodic Fe-defects, we also predict that single-layer $FeCl_3$, which we show is a dynamically stable AFM semiconductor, can be formed. Overall, our predictions reveal an understanding of the effect of defects, whose formations are inevitable during the synthesis of a 2D material, on the electronic properties of $FeCl_2$ at the atomic scale for future experiments.

ACKNOWLEDGMENTS

Computational resources were provided by TUBITAK ULAKBIM, High Performance and Grid Computing Center (TR-Grid e-Infrastructure), and by Flemish Supercomputer Center (VSC). H.S. acknowledges financial support from the Scientific and Technological Research Council of Turkey (TUBITAK) under Project No. 117F095. M.Y. was supported by the Flemish Science Foundation (FWO-Vl) by a postdoctoral fellowship.

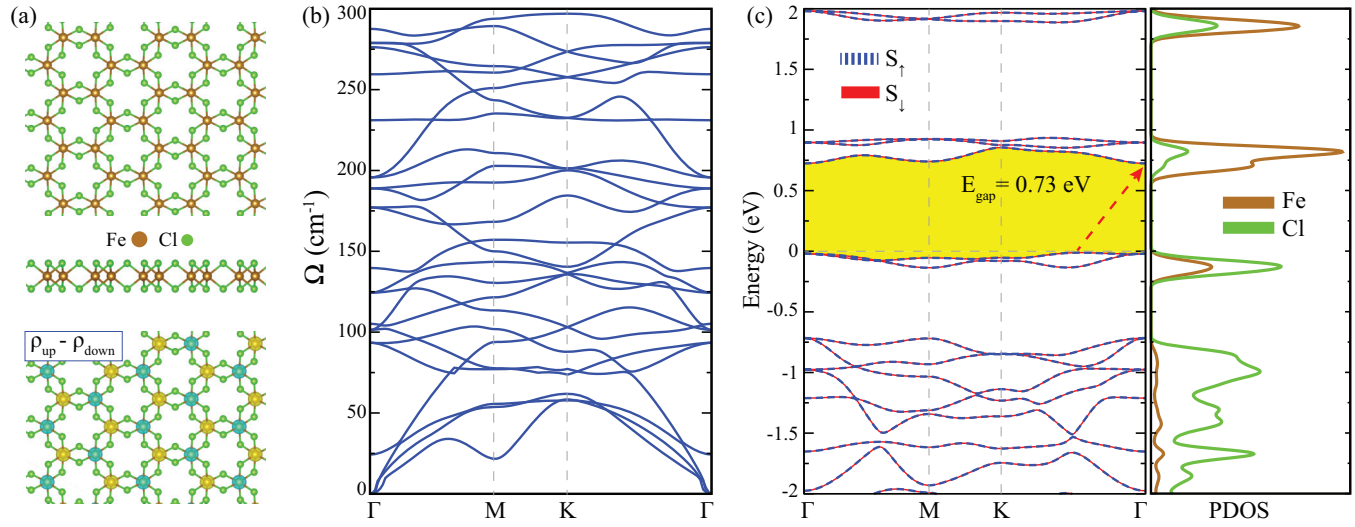

FIG. 5. Single-layer of $FeCl_3$: (a) Top, side views, and the charge-density difference. The blue and yellow spheres stand for the charge densities of opposite spins. (b) The phonon band structure through the whole Brillouin zone. (c) The electronic band structure and the corresponding PDOS for the AFM ground state. Dashed blue and solid red lines stand for opposite spin states, respectively.

[1] K. S. Novoselov, A. K. Geim, S. V. Morozov, D. Jiang, Y. Zhang, S. V. Dubonos, I. V. Grigorieva, and A. A. Firsov, Science **306**, 666 (2004).

[2] M. A. McGuire, H. Dixit, V. R. Cooper, and B. C. Sales, Chem. Mater. **27**, 612 (2015).

[3] S. Jiang, J. Shan, and K. F. Mak, Nat. Mater. **17**, 406 (2018).

[4] S. Jiang, L. Li, Z. Wang, K. F. Mak, and J. Shan, Nat. Nanotechnol. **13**, 549 (2018).

[5] W. Xing, Y. Chen, P. M. Odenthal, X. Zhang, W. Yuan, T. Su, Q. Song, T. Wang, J. Zhong, S. Jia, X. C. Xie, Y. Li, and W. Han, 2D Mater. **4**, 024009 (2017).

[6] F. Iyikanat, M. Yagmurcukardes, R. T. Senger, and H. Sahin, J. Mater. Chem. C **6**, 2019 (2018).

[7] J. A. Sears, M. Songvilay, K. W. Plumb, J. P. Clancy, Y. Qiu, Y. Zhao, D. Parshall, and Y.-J. Kim, Phys. Rev. B **91**, 144420 (2015).

[8] M. Bonilla, S. Kolekar, Y. Ma, H. C. Diaz, V. Kalappattil, R. Das, T. Eggers, H. R. Gutierrez, M. H. Pha, and M. Batzill, Nat. Nanotechnol. **13**, 289 (2018).

[9] P. M. Coelho, K. N. Cong, M. Bonilla, S. Kolkar, M. H. Phan, J. Avila, M. C. Asensio, I. I. Oleynik, and M. Batzill, J. Phys. Chem. C **123**, 14089 (2019).

[10] J. U. Lee, S. Lee, J. H. Ryoo, S. Kang, T. Y. Kim, P. Kim, C. H. Park, J. G. Park, and H. Cheong, Nano Lett. **16**, 7433 (2016).

[11] K.-z. Du, X.-z. Wang, Y. Liu, P. Hu, M. I. B. Utama, C. K. Gan, Q. Xiong, and C. Kloc, ACS Nano **10**, 1738 (2016).

[12] I. Eren, F. Iyikanat, and H. Sahin, Phys. Chem. Chem. Phys. **21**, 16718 (2019).

[13] J. He, S. Ma, P. Lyu, and P. Nachtigall, J. Mater. Chem. C **4**, 2518 (2016).

[14] E. Meloche and M. G. Cottam, Phys. Status Solidi **196**, 165 (2003).

[15] R. J. Birgeneau, W. B. Yelon, E. Cohen, and J. Makovsky, Phys. Rev. B **5**, 2607 (1972).

[16] E. Torun, H. Sahin, S. K. Singh, and F. M. Peeters, Appl. Phys. Lett. **106**, 192404 (2015).

[17] E. Torun, H. Sahin, C. Bacaksiz, R. T. Senger, and F. M. Peeters, Phys. Rev. B **92**, 104407 (2015).

[18] H. Zheng, J. Zheng, C. Wang, H. Han, and Y. Yan, J. Mag. Mag. Mat. **444**, 184 (2017).

[19] X. Zhou, B. Brzostowski, A. Durajsk, M. Liu, J. Xiang, T. Jiang, Z. Wang, S. Chen, P. Li, Z. Zhong, A. Drzewiski, M. Jarosik, R. Szczesniak, T. Lai, D. Guo, and D. Zhong, J. Phys. Chem. C **124**, 9416 (2020).

[20] W. Zhou, X. Zou, S. Najmaei, Z. Liu, Y. Shi, J. Kong, J. Lou, P. M. Ajayan, B. I. Yakobson, and J.-C. Idrobo, Nano Lett. **13**, 2615 (2013).

[21] H.-P. Komsa, J. Kotakoski, S. Kurasch, O. Lehtinen, U. Kaiser, and A. V. Krasheninnikov, Phys. Rev. Lett. **109**, 035503 (2012).

[22] X. Zou, Y. Liu, and B. I. Yakobson, Nano Lett. **13**, 253 (2013).

[23] Q. Yu, L. A. Jauregui, W. Wu, R. Colby, J. Tian, Z. Su, H. Cao, Z. Liu, D. Pandey, D. Wei, T. F. Chung, P. Peng, N. P. Guisinger, E. A. Stach, J. Bao, S.-S. Pei, and Y. P. Chen, Nat. Mater. **10**, 443 (2011).

[24] Y. Wei, J. Wu, H. Yin, X. Shi, R. Yang, and M. Dresselhaus, Nat. Mater. **11**, 759 (2012).

[25] F. Banhart, J. Kotakoski, and A. V. Krasheninniko, ACS Nano **5**, 26 (2011).

[26] J. Hong, Z. Hu, M. Probert, K. Li, D. Lv, X. Yang, L. Gu, N. Mao, Q. Feng, L. Xie, J. Zhang, D. Wu, Z. Zhang, C. Jin, W. Ji, X. Zhang, J. Yuan, and Z. Zhang, Nat. Commun. **6**, 6293 (2015).

[27] R. Wang, Y. Su, G. Yang, J. Zhang, and S. Zhang, Chem. Mater. **32**, 1545 (2020).

[28] M. Pizzochero, J. Phys. D **53**, 244003 (2020).

[29] G. Kresse and J. Hafner, Phys. Rev. B **47**, 558 (1993).

[30] G. Kresse and J. Furthmuller, Phys. Rev. B **54**, 11169 (1996).

[31] J. P. Perdew, K. Burke, and M. Ernzerhof, Phys. Rev. Lett. **77**, 3865 (1996).

[32] H. Sahin and S. Ciraci, J. Phys. Chem. C **116**, 24075 (2012).
[33] A. S. Botana and M. R. Norman, Phys. Rev. Mater. **3**, 044001 (2019).
[34] S. Cai, F. Yang, and C. Gao, Nanoscale **12**, 16041 (2020).
[35] M. Ashton, J. Paul, S. B. Sinnott, and R. G. Hennig, Phys. Rev. Lett. **118**, 106101 (2017).
[36] https://www.materialsweb.org.
[37] https://cmrdb.fysik.dtu.dk/c2db.